

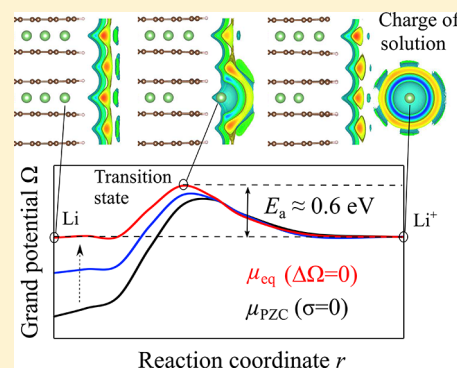
Analysis of Lithium Insertion/Desorption Reaction at Interfaces between Graphite Electrodes and Electrolyte Solution Using Density Functional + Implicit Solvation Theory

Jun Haruyama,*¹ Tamio Ikeshoji, and Minoru Otani*

Research Center for Computational Design of Advanced Functional Materials (CD-FMat), National Institute of Advanced Industrial Science and Technology (AIST), 1-1-1 Umezono, Tsukuba, Ibaraki 305-8568, Japan

Supporting Information

ABSTRACT: The charge transfer reaction at the electrode/solution interface is regarded as a major component that limits the current densities of Li-ion batteries. A combination of density functional theory for the electronic structure calculations of an electrode and a reacting component with implicit solvation theory for an electrolyte solution is used for the lithium insertion/desorption reaction (R). At the interfaces between tilted-graphite electrodes and a 1 M LiPF₆ ethylene carbonate solution, the energy landscapes of reaction R are revealed under constant electron chemical potential conditions. Across the transition state where the Li forms a half solvation shell, the reacting Li inside the electrode changes to a full solvation structure in the solution accompanied by electron transfer. On graphite with two tilt angles, the activation energies at the equilibrium potentials of reaction R are approximately 0.6 eV, which is consistent with the electrochemical impedance spectroscopy measurements. However, opposite-sign charges are obtained on the two angle surfaces, which can be well explained by the work functions on the tilted graphite. This study paves the way for the quantitative analysis of the charge-transfer reactions in electrochemical devices under electrochemically defined environments.



1. INTRODUCTION

Currently, to address problems associated with global warming and the depletion of fossil fuels, the energy conversion from renewable and sustainable energy sources to electrical power has become an essential technology. Rechargeable Li-ion batteries (LIBs) are promising candidates because of their outstanding properties such as high energy density and long cycle life.^{1–4} To increase their applicability, higher current densities in the charging and discharging processes are necessary. Electron transfer reactions at the electrodes, such as Li-insertion/desorption process and reductive/oxidative decomposition of organic electrolyte solutions, will play an important role to achieve the high current density. These processes are governed by the electrode potentials. The Li intercalation into a graphite is completed at 0.1–0.2 V relative to Li metal reference electrode (Li/Li⁺), while the reduction of solvents, such as ethylene carbonate (EC), ethyl methyl carbonate (EMC), dimethoxyethane (DME), dimethyl sulfide (DMSO), dimethyl carbonate (DMC), and their mixtures, starts at approximately 1 V vs Li/Li⁺.⁵ Graphite electrode passivation by the formation of solid electrolyte interphases (SEI) is necessary for continuous battery operation to prevent solvent degradation.^{6–8} To manage and control these electrochemical processes at electrode/solution interfaces, a quantitative understanding of elementary reactions in LIBs under well-defined electrode potentials is critical to achieve

innovative high-energy and high-current density rechargeable batteries.

Experimentally, electrochemical impedance spectroscopy (EIS) is often used to study the various processes under a controlled potential. EIS can distinguish between electron exchange and ion transfer that take place at electrode/solution interfaces and gives quantitative data for these processes.⁹ Zhang et al. showed that the total resistance of conventional LIB cells (graphite/LiPF₆ in EC/EMC/LiCoO₂) was able to be separated into three components: bulk solution, SEI, and predominant charge-transfer (CT) resistances.¹⁰ Abe et al. measured the temperature dependence of the CT resistances using their Li-ion cells (LiLiCF₃SO₃ in DME/DMSO/graphite) and obtained activation energies of 53–59 kJ/mol.¹¹ A subsequent experimental study reported almost the same value of 58 kJ/mol using an EC/DMC solution of LiClO₄.¹² Xu et al. showed the contribution to the CT barrier at the graphite electrode/solution interface from desolvation of Li⁺ and the subsequent migration of bare Li⁺ through SEI films.¹³ Consequently, a rate-determining CT process, which is characterized by an activation energy barrier of 50–70 kJ/mol, should occur when solvated Li⁺ intercalates the layered lattice of graphite; its primary Li⁺ solvated shell in an electrolyte

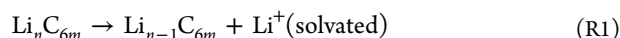
Received: February 27, 2018

Revised: April 6, 2018

Published: April 18, 2018

solution has to be broken down. These observations provide essential information for investigating the Li-insertion/desorption process at electrode/solution interfaces; however, more detailed analysis, microscopic measurements by operando spectroscopy and microscopic calculations as examples, are necessary toward a quantitative understanding of electrochemical reactions.

From the standpoint of computational studies, a general and consensual way of determining the potential on a single electrode in the first-principles treatment within periodic boundary conditions (PBC) has not yet been given. According to the definition of the electrode potential, the number of electrons N_e should change in a calculation cell to achieve the desired electron chemical potential μ_e . The change of N_e makes the total energy undefined as long as PBC are used. By applying *ab initio* molecular dynamics (AIMD) and thermodynamic integration techniques, Leung et al. calculated the free energy changes of Li^+ transfer between Li-intercalated graphite (LiC_6) and liquid EC solvent while changing the surface electron density and keeping the total number of electrons unchanged.^{14,15} They calculated the free energy difference ΔG of the following reaction:



A surface electron density corresponding to $\Delta G = 0$ could be interpreted as the onset of delithiation. These treatments, however, include a lot of difficulties, such as electronic structure modeling of solid–liquid interfaces, and the large computational cost of liquid dynamics at finite temperatures. Therefore, these problems make calculating the activation barriers of the CT reactions difficult for AIMD treatments.^{16,17}

In this study, we analyzed the Li insertion/desorption process (reaction R1) at the interface between a graphite electrode (tilted $\text{Li}_n\text{C}_{6m}\text{H}_l$) and EC-based electrolyte solution (1 M LiPF_6 EC). We employed density functional theory (DFT) calculations combined with the effective screening medium (ESM) technique¹⁸ + the reference interaction site model¹⁹ (RISM); ESM-RISM formulation simulates the graphite electrode and the electrolyte solution based on quantum mechanics (QM) and implicit classical solvation, respectively. We emphasize that the ESM-RISM simulation is able to realize the constant- μ_e conditions²⁰ because the number of electrons excluded to reach the target μ_e ($-\Delta N_e$) is always compensated by the distributions of the solvent, cations, and anions in the solution treated by the RISM equations.²¹ The total charge in the ESM-RISM system is neutral, and the inner potential at the bulk solution side can be defined. In this constant- μ_e condition, the free energy of the total system is no longer a well-behaved quantity for comparison; therefore, we should use grand potential Ω associated with reaction R1. The main objective of this study is to determine Ω along Li insertion/desorption paths at the $\text{Li}_n\text{C}_{6m}\text{H}_l$ /1 M LiPF_6 EC interfaces.

This article is organized as follows. Section 2 describes the ESM-RISM simulation, reaction R1 models at the $\text{Li}_n\text{C}_{6m}\text{H}_l$ /EC solution interfaces, and computational details. Section 3 shows Ω profiles at two characteristic μ_e levels on tilted graphite. Activation energies and transition states are also provided. The relation between the equilibrium potentials and electromotive forces and that between the surface charge density and work functions are discussed in Section 4. Finally, Section 5 provides the conclusions of this study.

2. METHODS AND MODELS

In the definition of grand potential $\Omega \equiv A - \mu_e N_e$, ESM-RISM describes the Helmholtz free energy A as

$$A = E_{\text{DFT}} + \Delta A_{\text{RISM}} \quad (1)$$

where E_{DFT} is the DFT total energy derived from the Kohn–Sham (KS) equation with the ESM open boundary condition.¹⁸ Self-consistent potentials, which arise from the interaction between electrons and RISM solvents,²² are considered in solving the KS equation. The excess free energy, which results from interactions between QM particles and the RISM solvents, is represented as ΔA_{RISM} . The distribution functions of RISM components, which refer to the reference sites of the RISM solvents, are determined by Laue-represented RISM equations.²¹ The interactions among the reference sites and QM ions (nucleus) are represented as Coulomb and Lennard–Jones (LJ) potentials.

ESM-RISM calculations were performed on the configuration of a vacuum/slab/solvent system as shown in Figure 1,

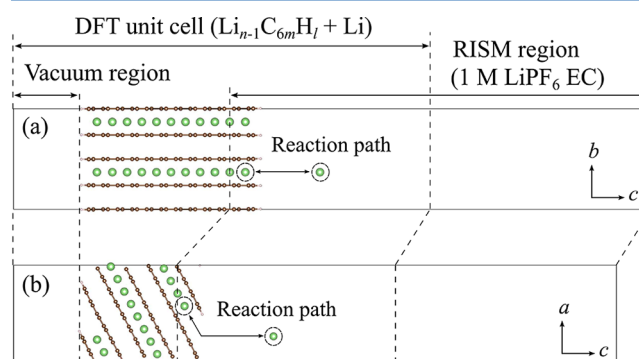


Figure 1. ESM-RISM configurations of the vacuum/slab/solvent system: the simulation cells of $\text{Li}_n\text{C}_{6m}\text{H}_l$ /1 M LiPF_6 EC interfaces tilted (a) 90° and (b) 30° . The H, Li, and C atoms are shown as white, light green, and brown spheres, respectively. The Li insertion/desorption paths are also indicated by two-direction arrows.

where the DFT slab domain is on the left-hand side, and the RISM solvents, that is, EC, Li^+ , and PF_6^- treated by the RISM equations, are on the right-hand side. When electrons were excluded to shift the μ_e level, the RISM solvents (molecules and ions) screened out the excess charge of the slab; the whole system kept the charge neutral condition. Since the salt concentration of typically 1.0 M in LIBs gives a small Debye screening length of several angstroms, the RISM region ($> \text{ca. } 40 \text{ \AA}$) used in the calculation was sufficiently long. Similar configuration systems, that is, vacuum/slab/implicit solvent system, were studied by several authors; surface redox potentials,²³ double layer structures,²⁴ and equilibrium potentials²⁵ have been discussed.

The Li insertion/desorption paths (reaction R1) were assumed as combinations of one or two straight lines, as indicated in Figure 1. The reacting Li was moved from the stable Li site in the graphite layer ($r = 0$) to the interior region of the solution. It is worth mentioning that the ESM-RISM simulation can define the inner potential; the electron chemical potentials μ_e applied in reaction R1 simulations against this inner potential can be converted to Li/Li^+ potentials on the Li metal reference electrode, which will be discussed in Section 4.

The procedures used for constructing surfaces of $\text{Li}_n\text{C}_{6m}\text{H}_l$ (tilted by 90° and 30° to the graphite basal planes) are

explained in the following. First, the bulk properties, such as cell parameters and formation energy, of AB stacked graphite, LiC_{12} , and LiC_6 were calculated with the Perdew–Burke–Ernzerhof (PBE) generalized-gradient approximation²⁶ and the van der Waals functional of the vdW-DF2-B86R²⁷ (vdW) as the exchange-correlation functional. Stacking layers and optimized lattice constants are shown in Figure S1 and Table S1 in the Supporting Information (SI). As revealed in the previous DFT calculations,^{28–31} PBE overestimated the c constant, that is, the interlayer distance, while vdW well reproduced the experimental lattice constants.^{32–34} Then, the electromotive force (E_{emf}) between discharged and charged states is represented as

$$E_{\text{emf}} = -\Delta G/nF \quad (2)$$

where n and F are the number of reacted electrons and Faraday constant, respectively. The free energy difference ΔG between discharged (LiC_6 or LiC_{12}) and charged states ($\text{Li} + \text{C}_6$ or $\text{Li} + \text{C}_{12}$) was approximated as the DFT energy difference ΔE between the states. The values of $-\Delta G$ or E_{emf} calculated from vdW-DFT, which are listed in Table S2, were close to the experimentally measured equilibrium potential of the Li_xC_6 ($0.5 \leq x \leq 1$) graphite electrode, that is, 0.1–0.2 V vs Li/Li^+ .^{35–37} Therefore, we conducted all of the calculations related to Ω and work functions by using the vdW functional.

We constructed the surface slabs of $\text{Li}_n\text{C}_{6m}\text{H}_l$ (tilted by 90° and 30° to the graphite basal plane) by cutting AA-stacked graphite crystals. Cell parameters after cutting were fixed at the optimized values of the AA-stacking LiC_6 or graphite bulk obtained with the vdW functional. Tilt angles of 90° , 60° , and 30° in this study correspond to the surface planes of $(1, \bar{1}, 0)$, $(1, \bar{1}, 1)$, and $(1, \bar{1}, 3)$, respectively. The influences of H , OH , and O terminations will be discussed in Section 5. Zigzag structures with H terminations were only applied for the calculations of reaction R1. All of the model $\text{Li}_n\text{C}_{6m}\text{H}_l$ structures, the stoichiometry, and cell parameters used in ESM-RISM simulations are shown in Figure S2 and Table S3, respectively. The slab thicknesses were approximately 2.5 and 1.5 nm for the 90° and 30° slabs, respectively; therefore, they were thick enough to show converged work functions with the ESM open boundary condition.

The parameters of classical force fields used for RISM calculations were selected from the literature as follows. Basically, the electrostatic potential (ESP) charges³⁸ and optimized potentials for liquid-phase simulation (OPLS)^{39,40} were used as the atomic charges and LJ parameters. These parameters of EC and PF_6^- were determined by reference to the reported values of Soetens et al. and Sambasivarao et al., respectively.^{41,42} Because the Li^+ solvation energy in the EC solution is directly linked to the stabilization of the reacting Li^+ state, the LJ parameters of Li^+ ion should be selected carefully. We used the proposed values⁴³ that give the correct free energy of hydration using generalized Born/surface area (GBSA)⁴⁴ calculations. The atomic structures of EC and PF_6^- are shown in Figure S3, and the parameters of the classical force fields for ESM-RISM simulations are listed in Tables S4 and S5. A 1D-RISM calculation¹⁹ using these parameters provided the Li^+ solvation energy in 1 M LiPF_6 EC of -4.14 eV, which is in good agreement with the previously calculated value of -3.96 eV.⁴⁵

2.1. Computational Details. Quantum ESPRESSO code^{46,47} was used to perform the spin-unpolarized DFT and ESM-RISM calculations, where the RISM part was implemented by Nishihara.²¹ A van der Waals^{48–50} exchange-

correlation functional of the vdW-DF2-B86R²⁷ (vdW) type was adopted with a plane-wave basis within the ultrasoft pseudopotential framework.^{51,52} The electronic configurations were $1s^1$ for H , $1s^2 2s^1$ for Li , $2s^2 2p^2$ for C , and $2s^2 2p^4$ for O with nonlinear core correction (NLCC).⁵³ The cutoff energies were set to 40 and 320 Ry (1 Ry = 13.606 eV) for the wave functions and the augmented charge, respectively. In the bcc Li calculations, the cutoff energies were increased to 80/640 Ry. The cutoff energies of 40 and 80 Ry provide converged DFT energies in Li -intercalated graphite and Li metal, respectively. Converged k -point sampling was adopted for the bulk and surface systems, whereas only the Γ point was chosen for the ESM-RISM interface systems. A vacuum region of 10 Å was added to the left-hand-side of all the $\text{Li}_n\text{C}_{6m}\text{H}_l$ slabs, and the C atoms closest to the left boundary were fixed in the ESM-RISM simulations. Electron occupation numbers were determined by the Gaussian smearing technique with a broadening parameter of 0.01 Ry. In the calculation along the Li insertion/desorption reaction paths, the atomic positions except the reacting Li atom were relaxed until the residual forces became less than 0.001 Ry/bohr (1 bohr = 0.52918 Å), while the cell parameters were fixed. The number of electrons was determined iteratively by the quasi-Newton method in which the convergence criterion (difference between target and calculated μ_e) was set to 0.01 eV. The solvent system was EC with a density of 1.32 g/cm³ (= 15.0 mol/L) and a temperature of 300 K. The Laue-RISM calculation was performed with the closure of the model of Kovalenko and Hirata,²² and the excess free energy ΔA_{RISM} was evaluated by the Gaussian fluctuation model, which is independent of the closure equation.⁵⁴ The cutoff energy was set to 160 Ry for the distribution functions of RISM components. The convergence criterion of the correlation functions in RISM equations was set to 10^{-6} Ry. The VESTA package was used to visualize the coordinates of the DFT atoms and the charge distributions of RISM components throughout this investigation.⁵⁵

3. RESULTS

3.1. Grand Potential Profiles. Figure 2a shows the profiles of the grand potential Ω along the reaction R1 path of 90° tilted graphite ($\text{Li}_{44}\text{C}_{576}\text{H}_{48}$) as indicated in Figure 1a. The number of excluded electrons $-\Delta N_e$ and electron chemical potentials μ_e in the simulations are shown in Figure S4a,b, respectively. The levels of μ_e were set at two different potentials. One was at the potential of zero charge (PZC), μ_{PZC} : the electron chemical potential calculated at the neutral slab of Li -intercalated graphite. The other was at the equilibrium potential, μ_{eq} , where the grand potential difference $\Delta\Omega$ in the reaction R1 must be equal to 0 at μ_{eq} . To determine μ_{eq} , μ_e was iteratively changed until $\Delta\Omega < 0.02$ eV.

On the Ω profile at μ_{PZC} for the 90° tilted graphite, $-\Delta N_e$ gradually increased as the reacting Li moved to the outside of the graphite and finally reached 0.96. The variation of N_e could be interpreted as Li changed to Li^+ at the solution side. The screening particles of the Li ion charge varied from the electrode electrons to the LiPF_6 electrolyte. Thus, the constant- μ_e ESM-RISM simulations along the reaction R1 path were accompanied by an electron transfer process. As shown in Figure S4a,b, μ_{eq} was set at the lower level compared with that of PZC, which resulted in the positive surface charge density σ^+ . Owing to the electrode positive charge, the double layer structure was changed from the neutral surface and the concentration of Li^+ ions decreased as indicated in Figure S5a.

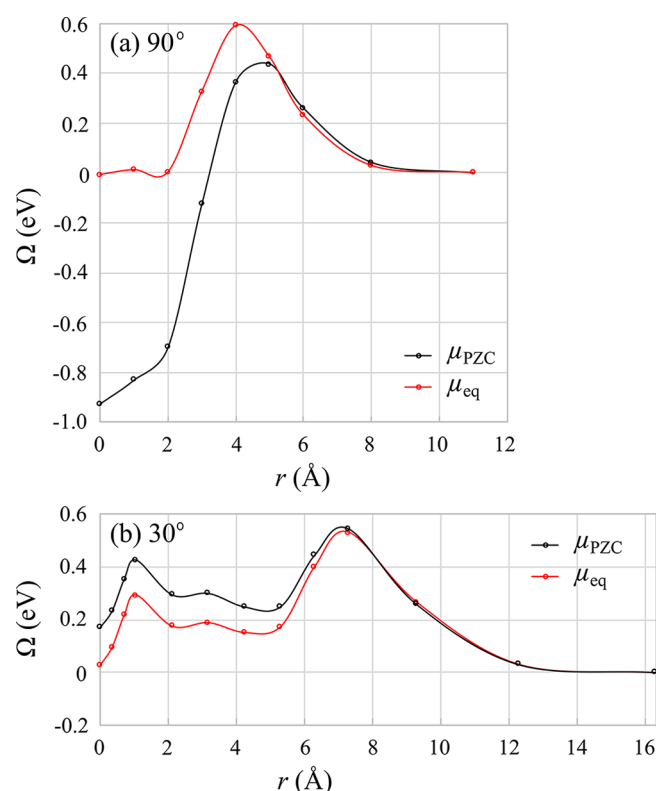


Figure 2. Profiles of grand potential Ω as a function of the reaction coordinate r : (a) 90° and (b) 30° tilted graphite as shown in Figure 1. The black and red circles show the values of Ω obtained by setting the chemical potentials at μ_{PZC} and μ_{eq} , respectively. The solid lines are depicted as a guide for the eye. The origin of Ω is set at the right-hand end of the Li reaction path.

Figure 2b presents the Ω profiles on the reaction R1 path of 30° tilted graphite ($\text{Li}_{24}\text{C}_{432}\text{H}_{24}$) as shown in Figure 1b. The numbers of excluded electrons $-\Delta N_e$, electron chemical potentials μ_e , and concentrations of the EC solvent and LiPF_6 electrolyte are also shown in Figures S4c,d and S5b, respectively. For the reaction under the PZC, $-\Delta N_e$ changed from 0 to 0.93; the state of the reacting Li varied from Li to Li^+ . The reaction barrier occurred around $r = 1$ Å when the reacting Li crossed between the vertices of the hexagonal C lattice, see Figure S6. The next two stable regions at around 2 and 5 Å appeared at the Li adsorption sites located just above the side and center of the C hexagon, respectively. To realize the equilibrium potential, μ_{eq} was set at a slightly higher value compared with μ_{PZC} . The negative surface charge density σ^- was obtained at μ_{eq} in contrast to 90° tilted graphite; detailed explanation will be presented in Section 5.

3.2. Activation Energies. Transition state energies, that is, those at the maximum points in Ω profiles, at $r = 4.0$ and 7.3 Å were 0.59 and 0.53 eV on 90° and 30° tilted graphite, respectively. These energies could be regarded as the activation energies derived from ESM-RISM calculations with the constant- μ_{eq} condition and were consistent with the reported CT barriers obtained from EIS measurements.^{10–13} The charge distributions of the RISM solvents at the transition states of reaction R1 are visualized in Figure 3. Additionally, Figures S7 and S8 show the charge distributions at the start and end of reaction R1 on 90° and 30° tilted graphite, respectively. When the reacting Li was placed in the bulk solution region, the EC solvent and LiPF_6 electrolyte formed spherical distributions

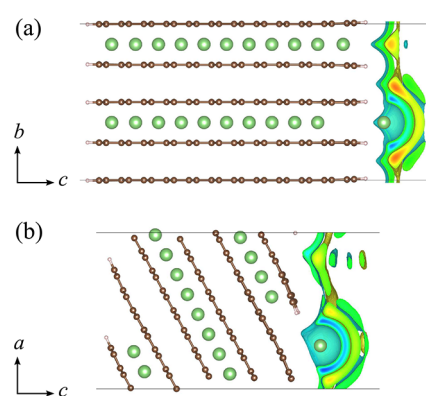


Figure 3. Charge distributions of the RISM solvents around the reacting Li atom at the transition states with constant- μ_{eq} conditions: (a) 90° and (b) 30° tilted graphite.

around Li^+ as shown in Figures S7c and S8c. The formations of the perfect spherical solvation structure broke down at the transition states because of surface interactions, which led to hemispherical structures. These half solvation shells corresponded to the experimental indication that the desolvation process was the main origin of the large activation energy of the CT resistance.

In addition to the above results, similar reaction profiles were obtained by changing the Li composition ratios, as indicated in Figure S2 and Table S3. We labeled the different stoichiometry models in the order of increasing Li content; the indices of 90° and 30° tilted graphite were A–D and E–F, respectively. A (E) was the insertion/desorption model in which reacting Li entered to Li-empty graphite. B (F) was the same as the interface model indicated in Figure 1 (LiC_{12} model). Because the Li atoms, which are located out of the graphite C edges, were removed, the Li/C ratios of the LiC_{12} models were smaller than the exact LiC_{12} stoichiometry. C (G) had almost the same composition ratio as the LiC_{12} model, but the reacting Li was inserted into an Li-empty layer. The D (H) was the insertion/desorption model of fully lithiated graphite (LiC_6 model). The activation energies E_a of reaction R1 with constant- μ_{eq} conditions and corresponding Ω profiles are presented in Table 1 and Figure S9, respectively. The difference of E_a among

Table 1. Activation Energies E_a , Equilibrium Chemical Potentials μ_{eq} , and Surface Charge Densities σ

angle [deg]	index	stoichiometry	E_a [eV]	μ_{eq} [eV]	σ [e/nm ²]
90	A	$\text{Li}_1\text{C}_{576}\text{H}_{48}$	0.65	−4.22	0.46
	B	$\text{Li}_{44}\text{C}_{576}\text{H}_{48}$	0.59	−3.85	0.40
	C	$\text{Li}_{45}\text{C}_{576}\text{H}_{48}$	0.62	−3.60	0.32
	D	$\text{Li}_{88}\text{C}_{576}\text{H}_{48}$	0.58	−3.45	0.33
30	E	$\text{Li}_1\text{C}_{432}\text{H}_{24}$	0.64	−3.76	−0.07
	F	$\text{Li}_{24}\text{C}_{432}\text{H}_{24}$	0.53	−3.56	−0.06
	G	$\text{Li}_{25}\text{C}_{432}\text{H}_{24}$	0.52	−3.23	−0.20
	H	$\text{Li}_{48}\text{C}_{432}\text{H}_{24}$	0.67	−3.00	−0.20

all the models was within 0.15 eV. The activation barriers had small dependences on the graphite tilt angles and on the Li composition ratios because all of the transition states were located at similar desolvation points where the solvated Li^+ entered the graphite layer. Table 1 also listed μ_{eq} and the surface charge densities σ at $r = 0$. The decreasing of μ_{eq} as the Li content increased was consistent with the thermodynami-

cally interpreted downward shift of the intercalation potential of Li_xC_6 as the composition ratio x increased.^{35–37}

4. DISCUSSION

In the ESM-RISM calculations, the chemical potential of an electron, μ_e , was measured from the inner solvent potential Φ_{solv} at the bulk solution region (i.e., the right-hand side of the simulation cell in Figure 1). If the same electrolyte solution is used, Φ_{solv} does not change even though the electrode reaction changes; therefore, Φ_{solv} can be used as a reference potential for the electrochemical cell in the same manner as the reference electrode used in the experiments. As a result, it is possible to compare μ_e at different electrodes contacting the same solution directly. The difference between two equilibrium potentials on different electrodes, $\Delta\mu_{\text{eq}}$, provides the electromotive force, E_{emf} between the two electrodes as

$$E_{\text{emf}} = -\Delta\mu_{\text{eq}}/e \quad (3)$$

where e is the elementary charge. Once the equilibrium potential $\mu_{\text{Li/Li}^+}$ of the reaction Li/Li^+ , that is, Li transfer reaction at the Li metal electrode, is determined in the ESM-RISM calculation, the electrode potential relative to the Li/Li^+ reference can be obtained. When the distance between an electrode surface and the solvated Li^+ was large enough to ignore the interaction between them, both eqs 2 and 3 gave the same E_{emf} from the ESM-RISM calculations.

Filhol et al. have already calculated the Li/Li^+ equilibrium potential at a $\text{Li}(110)$ surface by combining DFT calculations with the polarizable continuum model.²⁵ Using the force field parameters described in Section 2 and the DFT energy of bcc Li metal, we obtained $\mu_{\text{Li/Li}^+} = -3.0$ eV versus Φ_{solv} of 1 M LiPF_6 EC. It should be noted that, using this $\mu_{\text{Li/Li}^+}$, the equilibrium potentials of the simulated $\text{Li}_x\text{C}_{6m}\text{H}_l$ slabs showed slightly higher values compared with the intercalation potential of Li_xC_6 , 0.1–0.2 V vs Li/Li^+ .^{35–37} For example, the equilibrium potential of the LiC_{12} model labeled B and F in Table 1 was approximately 0.8 and 0.5 V vs Li/Li^+ , respectively. These differences mainly arose from the stability of the reacting Li site, which could be estimated by calculating the vacancy formation energies $E(V_{\text{Li}})$ as

$$E(V_{\text{Li}}) = -\{A(\text{Li}_n\text{C}_{6m}\text{H}_l) - A(\text{Li}_{n-1}\text{C}_{6m}\text{H}_l) - E_{\text{DFT}}(\text{bcc Li})\} \quad (4)$$

where A and E_{DFT} are the Helmholtz free energy and DFT total energy in eq 1, respectively. The $\text{Li}_{n-1}\text{C}_{6m}\text{H}_l$ slab was simply prepared by extracting one Li atom from the i -th layer. Table S6 shows $E(V_{\text{Li}})$ for the B and F models. The reacting Li placed at the edge site, as shown in Figure 1, that is, first layer Li, was less stable compared with the inner Li sites.

An opposite sign of the surface charge densities was observed, as shown in Table 1, between the 90° and 30° tilted graphite. To explain this, we calculated the work functions Φ with respect to the graphite tilt angles for H-, OH-, and O-termination and of the basal c plane as shown in Figure 4. The graphite slabs used in the calculations for the work functions are shown in Figure S10. The value of $\Phi = 4.43$ eV of the c plane is comparable with the experiments and previous DFT calculations (4.5–4.6 eV).^{56–58} The work functions of 90° (3.40, 3.00, and 8.50 eV for H-, OH-, and O-termination, respectively) were also comparable with those of the graphene edges.⁵⁹ From these comparable results, the Φ values obtained here are quite reliable for the following discussion. As far as we

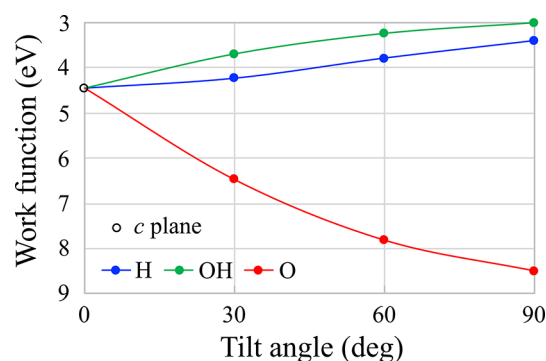


Figure 4. Work functions as a function of graphite tilt angle. The open, blue, green, and red circles represent the values of the c plane and H-, OH-, and O-termination slabs, respectively.

know, the work function calculations other than for 0° and 90° have not been reported before. The Φ of 30° and 60° clearly showed the intermediate tendency between 0° and 90° . We confirmed that Li intercalated graphite (Li_xC_6) showed lower Φ (about a few tenths of eV) compared with pristine graphite, as shown in Figure 4, although the presence of Li adsorptions substantially decreased the work functions.

From the H-termination results presented in Figure 4, electrons on the perpendicular plane (90°) could easily escape from the surface (small Φ), while those on the basal plane (0°) were difficult to extract (large Φ). If the polarization of the double layer is small, the Fermi energies (vs vacuum level, i.e., the negative of Φ) are a good approximation of μ_{PZC} . Thus, μ_{PZC} is highly dependent on the tilt angles, in contrast to the small dependency of μ_{eq} on the tilt angles. Consequently, the surface charge densities required to reach the target μ_{eq} levels were different between 90° and 0° tilted graphite. If μ_{PZC} is higher than that of μ_{eq} (90° case), the electrons should be extracted from the surface and vice versa. From the work function dependencies of tilt angles in Figure 4, the basal plane surface is expected to be more negatively charged compared with that of 30° ; the charge density is consistent with the previous results obtained by Leung and Tenney.¹⁴ Since the double layer structures (e.g., Li^+ concentration profile) were significantly different between positively and negatively charged surfaces, as shown in Figure S5, we can expect that the CT current is dependent on the tilt angles (more precisely, the work functions) of graphite surfaces (see the current–overpotential equation in ref 60).

Finally, reaction R1 in the presence of SEI as a graphite/SEI/solution is discussed. In this study, we showed that reaction R1 was accompanied by a desolvation process. Quantitatively, the activation barrier related with reaction R1 would not be changed, if it occurs on the solution side. At the SEI/solution interface, the transition state is expected to be similar to that at the graphite/solution interfaces, which will result in the same activation energy as the graphite/solution interface. In contrast to the desolvation process, an electron transfer process would occur at the graphite/SEI interface because the insulating property of SEI is not able to supply additional electrons to compensate for the Li^+ charge inside the insulating layer. Therefore, the desolvation process at SEI/solution interfaces is no longer accompanied by a CT process. In this context, it would be of great interest to investigate reaction R1 at an electrode/SEI/solution interface.

5. CONCLUSIONS

We conducted the Li insertion/desorption simulation at the interfaces between tilted $\text{Li}_n\text{C}_{6m}\text{H}_l$ graphite electrodes and 1 M LiPF_6 EC solution. Applying the ESM-RISM simulation with constant- μ_e conditions, the Li transfer path at the interface was found to be accompanied by CT reactions according to the changes of the number of electrons on the electrode. We obtained the grand potential landscapes for the CT reaction paths at the equilibrium potentials. Their activation barriers were approximately 0.6 eV for all tilted graphite samples examined, which were consistent with experiments. Furthermore, the RISM solvent and ions were automatically distributed in the half solvating structures at the transition state. At the equilibrium potentials for the CT reaction, the surface charge densities strongly depended on the tilt angles of graphite, which could be well explained by the work functions of the tilted graphite surfaces. This study establishes a method that includes the CT reaction at electrode/solution interfaces under well-defined electrochemical conditions and paves the way to a quantitative analysis for the performance of electrochemical devices related with CT reactions.

■ ASSOCIATED CONTENT

Supporting Information

The Supporting Information is available free of charge on the ACS Publications website at DOI: 10.1021/acs.jpcc.8b01979.

Bulk atomic structures and cell parameters of AB-stacked graphite, LiC_{12} , and LiC_6 . Free energy differences and electromotive forces between discharged and charged states. Configurations of atomic structures, unit cells, model indices, and cell parameters of the $\text{Li}_n\text{C}_{6m}\text{H}_l$ slabs for ESM-RISM simulations. Reference sites of EC and PF_6^- . Effective charges and Lennard-Jones parameters. Numbers of excluded electrons and chemical potential of 90° and 30° tilted graphite. Double layer structures of the RISM solvents. Configuration of the Li reaction path of 30° graphite. Charge distributions of the RISM solvents. Profiles of grand potential of various stoichiometry models. Vacancy formation energies for LiC_{12} model slabs. Atomic structures of 0° , 30° , 60° , and 90° graphite slabs for the calculation of work functions (PDF)

■ AUTHOR INFORMATION

Corresponding Authors

*E-mail: haruyama-jun@aist.go.jp.

*E-mail: minoru.otani@aist.go.jp.

ORCID

Jun Haruyama: 0000-0003-2310-4104

Notes

The authors declare no competing financial interest.

■ ACKNOWLEDGMENTS

This work was supported by the R&D Initiative for scientific innovation of new generation batteries 2 Project (RISING2) administrated by the New Energy and Industrial Technology Department Organization (NEDO). This work was also supported in part by JSPS KAKENHI Grant Number JP16K17969. The calculations were conducted on the K computer through the HPCI System Research Project (Project

ID: hp170117) as well as the supercomputers in The University of Tokyo and Nagoya University.

■ REFERENCES

- (1) Armand, M.; Tarascon, J.-M. Building Better Batteries. *Nature* **2008**, *451*, 652–657.
- (2) Li, B. H.; Wang, Z.; Chen, L.; Huang, X. Research on Advanced Materials for Li-Ion Batteries. *Adv. Mater.* **2009**, *21*, 4593–4607.
- (3) Etacheri, V.; Marom, R.; Elazari, R.; Salitra, G.; Aurbach, D. Challenges in the Development of Advanced Li-Ion Batteries: A Review. *Energy Environ. Sci.* **2011**, *4*, 3243–3262.
- (4) Goodenough, J. B.; Park, K.-S. The Li-Ion Rechargeable Battery: A Perspective. *J. Am. Chem. Soc.* **2013**, *135*, 1167–1176.
- (5) Zhang, X.; Kostecki, R.; Richardson, T. J.; Pugh, J. K.; Ross, P. N. Electrochemical and Infrared Studies of the Reduction of Organic Carbonates. *J. Electrochem. Soc.* **2001**, *148*, A1341–A1345.
- (6) Xu, K. Electrolytes and Interphases in Li-Ion Batteries and Beyond. *Chem. Rev.* **2014**, *114*, 11503–11618.
- (7) An, S. J.; Li, J.; Daniel, C.; Mohanty, D.; Nagpure, S.; Wood, D. L. The State of Understanding of the Lithium-Ion-Battery Graphite Solid Electrolyte Interphase (SEI) and Its Relationship to Formation Cycling. *Carbon* **2016**, *105*, 52–76.
- (8) Li, Y.; Leung, K.; Qi, Y. Computational Exploration of the Li-Electrode/Electrolyte Interface in the Presence of a Nanometer Thick Solid-Electrolyte Interphase. *Acc. Chem. Res.* **2016**, *49*, 2363–2370.
- (9) Dolle, M.; Orsini, F.; Gozdz, A. S.; Tarascon, J.-M. Development of Reliable Three-Electrode Impedance Measurements in Plastic Li-Ion Batteries. *J. Electrochem. Soc.* **2001**, *148*, A851–A857.
- (10) Zhang, S. S.; Xu, K.; Jow, T. R. Electrochemical Impedance Study on the Low Temperature of Li-Ion Batteries. *Electrochim. Acta* **2004**, *49*, 1057–1061.
- (11) Abe, T.; Fukuda, H.; Iriyama, Y.; Ogumi, Z. Solvated Li-Ion Transfer at Interface Between Graphite and Electrolyte. *J. Electrochem. Soc.* **2004**, *151*, A1120–A1123.
- (12) Yamada, Y.; Iriyama, Y.; Abe, T.; Ogumi, Z. Kinetics of Lithium Ion Transfer at the Interface between Graphite and Liquid Electrolytes: Effects of Solvent and Surface Film. *Langmuir* **2009**, *25*, 12766–12770.
- (13) Xu, K.; von Cresce, A.; Lee, U. Differentiating Contributions to “Ion Transfer” Barrier from Interphasial Resistance and Li^+ Desolvation at Electrolyte/Graphite Interface. *Langmuir* **2010**, *26*, 11538–11543.
- (14) Leung, K.; Tenney, C. M. Toward First Principles Prediction of Voltage Dependences of Electrolyte/Electrolyte Interfacial Processes in Lithium Ion Batteries. *J. Phys. Chem. C* **2013**, *117*, 24224–24235.
- (15) Leung, K. Predicting the Voltage Dependence of Interfacial Electrochemical Processes at Lithium-Intercalated Graphite Edge Planes. *Phys. Chem. Chem. Phys.* **2015**, *17*, 1637–1643.
- (16) Ikeshoji, T.; Otani, M. Towards Full Simulation of the Electrochemical Oxygen Reduction Reaction on Pt Using First-Principles and Kinetic Calculations. *Phys. Chem. Chem. Phys.* **2017**, *19*, 4447–4453.
- (17) Ohwaki, T.; Ozaki, T.; Okuno, Y.; Ikeshoji, T.; Imai, H.; Otani, M. Li Deposition and Desolvation with Electron Transfer at a Silicon/Propylene-Carbonate Interface: Transition-State and Free-Energy Profiles by Large Scale First-Principles Molecular Dynamics. *Phys. Chem. Chem. Phys.* **2018**, DOI: 10.1039/C7CP08569A.
- (18) Otani, M.; Sugino, O. First-Principles Calculations of Charged Surfaces and Interfaces: A Plane-Wave Nonrepeated Slab Approach. *Phys. Rev. B: Condens. Matter Mater. Phys.* **2006**, *73*, 115407.
- (19) Hirata, F.; Rossky, P. J. An Extended RISM Equation for Molecular Polar Fluids. *Chem. Phys. Lett.* **1981**, *83*, 329–334.
- (20) Bonnet, N.; Morishita, T.; Sugino, O.; Otani, M. First-Principles Molecular Dynamics at a Constant Electrode Potential. *Phys. Rev. Lett.* **2012**, *109*, 266101.
- (21) Nishihara, S.; Otani, M. Hybrid Solvation Models for Bulk, Interface, and Membrane: Reference Interaction Site Methods Coupled with Density Functional Theory. *Phys. Rev. B: Condens. Matter Mater. Phys.* **2017**, *96*, 115429.

- (22) Kovalenko, A.; Hirata, F. Self-Consistent Description of a Metal–Water Interface by the Kohn–Sham Density Functional Theory and the Three-Dimensional Reference Interaction Site Model. *J. Chem. Phys.* **1999**, *110*, 10095–10112.
- (23) Jinnouchi, R.; Anderson, A. B. Aqueous and Surface Redox Potentials from Self-Consistently Determined Gibbs Energies. *J. Phys. Chem. C* **2008**, *112*, 8747–8750.
- (24) Luque, N. B.; Woelki, S.; Henderson, D.; Schmickler, W. A Model for the Electrical Double Layer Combining Integral Equation Techniques with Quantum Density Functional Theory. *Electrochim. Acta* **2011**, *56*, 7298–7302.
- (25) Lespes, N.; Filhol, J.-S. Using Implicit Solvent in *Ab Initio* Electrochemical Modeling: Investigating Li⁺/Li Electrochemistry at a Li/Solvent Interface. *J. Chem. Theory Comput.* **2015**, *11*, 3375–3382.
- (26) Perdew, J. P.; Burke, K.; Ernzerhof, M. Generalized Gradient Approximation Made Simple. *Phys. Rev. Lett.* **1996**, *77*, 3865–3868.
- (27) Hamada, I. Van der Waals Density Functional Made Accurate. *Phys. Rev. B: Condens. Matter Mater. Phys.* **2014**, *89*, 121103.
- (28) Kganyago, K. R.; Ngoepe, P. E. Structural and Electronic Properties of Lithium Intercalated Graphite LiC₆. *Phys. Rev. B: Condens. Matter Mater. Phys.* **2003**, *68*, 205111.
- (29) Thinius, S.; Islam, M. M.; Heitjans, P.; Bredow, T. Theoretical Study of Li Migration in Lithium–Graphite Intercalation Compounds with Dispersion-Corrected DFT Methods. *J. Phys. Chem. C* **2014**, *118*, 2273–2280.
- (30) Wang, Z.; Selbach, S. M.; Grande, T. Van der Waals Density Functional Study of the Energetics of Alkali Metal Intercalation in Graphite. *RSC Adv.* **2014**, *4*, 4069–4079.
- (31) Ganesh, P.; Kim, J.; Park, C.; Yoon, M.; Reboredo, F. A.; Kent, P. R. C. Binding and Diffusion of Lithium in Graphite: Quantum Monte Carlo Benchmarks and Validation of van der Waals Density Functional Methods. *J. Chem. Theory Comput.* **2014**, *10*, 5318–5323.
- (32) Guerard, D.; Herold, A. Intercalation of Lithium into Graphite and Other Carbons. *Carbon* **1975**, *13*, 337–345.
- (33) Sumiyoshi, Y.; Ushio, M.; Suzuki, S. Formation of Graphite Single Crystal from Iron Solution by the Slow Cooling Method. *Bull. Chem. Soc. Jpn.* **1988**, *61*, 1577–1585.
- (34) Wang, X.-L.; An, K.; Cai, L.; Feng, Z.; Nagler, S. E.; Daniel, C.; Rhodes, K. J.; Stoica, A. D.; Skorpenske, H. D.; Liang, C.; et al. Visualizing the Chemistry and Structure Dynamics in Lithium-Ion Batteries by *In-Situ* Neutron Diffraction. *Sci. Rep.* **2012**, *2*, 747.
- (35) Churikov, A. V.; Ivanishev, A. V. Application of Pulse Methods to the Determination of the Electrochemical Characteristics of Lithium Intercalates. *Electrochim. Acta* **2003**, *48*, 3677–3691.
- (36) Levi, M. D.; Markevich, E.; Aurbach, D. Comparison between Cottrell Diffusion and Moving Boundary Models for Determination of the Chemical Diffusion Coefficients in Ion-Insertion Electrodes. *Electrochim. Acta* **2005**, *51*, 98–110.
- (37) Gallagher, K. G.; Dees, D. W.; Jansen, A. N.; Abraham, D. P.; Kang, S.-H. A Volume Averaged Approach to the Numerical Modeling of Phase-Transition Intercalation Electrodes Presented for Li_xC₆. *J. Electrochem. Soc.* **2012**, *159*, A2029–A2037.
- (38) Singh, U. C.; Kollman, P. A. An Approach to Computing Electrostatic Charges for Molecules. *J. Comput. Chem.* **1984**, *5*, 129–145.
- (39) Jorgensen, W. L.; Tirado-Rives, J. The OPLS Potential Functions for Proteins. Energy Minimizations for Crystals of Cyclic Peptides and Crambin. *J. Am. Chem. Soc.* **1988**, *110*, 1657–1666.
- (40) Jorgensen, W. L.; Maxwell, D. S.; Tirado-Rives, J. Development and Testing of the OPLS All-Atom Force Field on Conformational Energetics and Properties of Organic Liquids. *J. Am. Chem. Soc.* **1996**, *118*, 11225–11236.
- (41) Soetens, J.-C.; Millot, C.; Maigret, B. Molecular Dynamics Simulation of Li⁺BF₄[−] in Ethylene Carbonate, Propylene Carbonate, and Dimethyl Carbonate Solvents. *J. Phys. Chem. A* **1998**, *102*, 1055–1061.
- (42) Sambasivarao, S. V.; Acevedo, O. Development of OPLS-AA Force Field Parameters for 68 Unique Ionic Liquids. *J. Chem. Theory Comput.* **2009**, *5*, 1038–1050.
- (43) <https://github.com/thatchristoph/vmd-cvs-github/blob/master/plugins/bossconvert/oplsaa.par> (accessed April 5, 2018).
- (44) Jorgensen, W. L.; Ulmschneider, J. P.; Tirado-Rives, J. Free Energies of Hydration from a Generalized Born Model and an All-Atom Force Field. *J. Phys. Chem. B* **2004**, *108*, 16264–16270.
- (45) Cui, W.; Lansac, Y.; Lee, H.; Hong, S.-T.; Jang, Y. H. Lithium Ion Solvation by Ethylene Carbonates in Lithium-Ion Battery Electrolytes, Revisited by Density Functional Theory with the Hybrid Solvation Model and Free Energy Correction in Solution. *Phys. Chem. Chem. Phys.* **2016**, *18*, 23607–23612.
- (46) Giannozzi, P.; Baroni, S.; Bonini, N.; Calandra, M.; Car, R.; Cavazzoni, C.; Ceresoli, D.; Chiarotti, G. L.; Cococcioni, M.; Dabo, I.; et al. QUANTUM ESPRESSO: A Modular and Open-Source Software Project for Quantum Simulations of Materials. *J. Phys.: Condens. Matter* **2009**, *21*, 395502.
- (47) Giannozzi, P.; Andreussi, O.; Brumme, T.; Bunau, O.; Nardelli, M. B.; Calandra, M.; Car, R.; Cavazzoni, C.; Ceresoli, D.; Cococcioni, M.; et al. Advanced Capabilities for Materials Modeling with QUANTUM ESPRESSO. *J. Phys.: Condens. Matter* **2017**, *29*, 465901.
- (48) Dion, M.; Rydberg, H.; Schröder, E.; Langreth, D. C.; Lundqvist, B. I. Van der Waals Density Functional for General Geometries. *Phys. Rev. Lett.* **2004**, *92*, 246401.
- (49) Berland, K.; Cooper, V. R.; Lee, K.; Schröder, E.; Thonhauser, T.; Hyldgaard, P.; Lundqvist, B. I. Van der Waals Forces in Density Functional Theory: A Review of the vdW-DF Method. *Rep. Prog. Phys.* **2015**, *78*, 066501.
- (50) Thonhauser, T.; Zuluaga, S.; Arter, C. A.; Berland, K.; Schröder, E.; Hyldgaard, P. Spin Signature of Nonlocal Correlation Binding in Metal–Organic Frameworks. *Phys. Rev. Lett.* **2015**, *115*, 136402.
- (51) Vanderbilt, D. Soft Self-Consistent Pseudopotentials in a Generalized Eigenvalue Formalism. *Phys. Rev. B: Condens. Matter Mater. Phys.* **1990**, *41*, 7892–7895.
- (52) Rappe, A. M.; Rabe, K. M.; Kaxiras, E.; Joannopoulos, J. D. Optimized Pseudopotentials. *Phys. Rev. B: Condens. Matter Mater. Phys.* **1990**, *41*, 1227–1230.
- (53) Louie, S. G.; Froyen, S.; Cohen, M. L. Nonlinear Ionic Pseudopotentials in Spin-Density-Functional Calculations. *Phys. Rev. B: Condens. Matter Mater. Phys.* **1982**, *26*, 1738–1742.
- (54) Chandler, D.; Singh, Y.; Richardson, D. M. Excess Electrons in Simple Fluids. I General Equilibrium Theory for Classical Hard Sphere Solvents. *J. Chem. Phys.* **1984**, *81*, 1975–1982.
- (55) Momma, K.; Izumi, F. VESTA: A Three-Dimensional Visualization System for Electronic and Structural Analysis. *J. Appl. Crystallogr.* **2011**, *44*, 1272–1276.
- (56) Moos, G.; Gahl, C.; Fasel, R.; Wolf, M.; Hertel, T. Anisotropy of Quasiparticle Lifetimes and the Role of Disorder in Graphite from Ultrafast Time-Resolved Photoemission Spectroscopy. *Phys. Rev. Lett.* **2001**, *87*, 267402.
- (57) Hibino, H.; Kageshima, H.; Kotsugi, M.; Maeda, F.; Guo, F.-Z.; Watanabe, Y. Dependence of Electronic Properties of Epitaxial Few-Layer Graphene on the Number of Layers Investigated by Photoelectron Emission Microscopy. *Phys. Rev. B: Condens. Matter Mater. Phys.* **2009**, *79*, 125437.
- (58) Ooi, N.; Rairkar, A.; Adams, J. B. Density Functional Study of Graphite Bulk and Surface Properties. *Carbon* **2006**, *44*, 231–242.
- (59) Wang, W.; Li, Z. Potential Barrier of Graphene Edges. *J. Appl. Phys.* **2011**, *109*, 114308.
- (60) Bard, A. J.; Faulkner, L. R. *Electrochemical Methods: Fundamentals and Applications*; Wiley: New York, 1980.